Stabilization of a Two-Dimensional Hypersonic Boundary Layer Using a Shallow Cavity

Jiaao Hao[a] and Chih-Yung Wen[a,b,*]

[a] Department of Mechanical Engineering, The Hong Kong Polytechnic University, Kowloon, Hong Kong

[b] Interdisciplinary Division of Aeronautical and Aviation Engineering, The Hong Kong Polytechnic University, Kowloon, Hong Kong

Abstract

The stability of a two-dimensional hypersonic flat-plate boundary layer with a shallow cavity is investigated at Mach 6 using direct numerical simulations. The boundary layer is perturbed by a single-frequency wall blowing-suction actuator. The results indicate that the second mode is damped when the cavity is placed slightly downstream of the synchronization point (SP) of mode F and mode S, whereas the effect is reversed if it is located upstream or further downstream. The effect of the cavity depth is also studied. Strong damping of the second-mode disturbance is observed across the cavity. Energy budget analysis reveals that the presence of a shear layer bridging the leading and trailing edges of the cavity significantly reduces the work done by the Reynolds stress on the mean velocity gradient, which derives energy from the base flow and is the major contributor to the second-mode amplification near the flat-plate surface. It is suggested that a boundary layer dominated by second-mode instabilities can be efficiently stabilized by placement of a shallow cavity in the near-downstream region of the SP associated with the most amplified frequency. The damping effect depends on the cavity depth with a trend similar to that for hypersonic boundary layers over ultrasonically absorptive coatings, despite the fact that the flow structures can be very different.

Corresponding author
Email address: cywen@polyu.edu.hk

Nomenclature

c = nondimensional phase velocity

C_v = specific heat at constant volume, J/kg/K

d = cavity depth, mm

e = total energy per unit mass, J/kg

E = energy norm per unit volume, J/m^3

f = frequency, kHz

h = total enthalpy per unit mass, J/kg

k = disturbance energy, J/kg

l = cavity length, mm

M = Mach number

p = pressure, Pa

Pr = Prandtl number

q_i = vector of heat conduction, J/m^2/s

R = gas constant, J/kg/K

Re = Reynolds number

T = temperature, K

u_i = flow velocity, m/s

α = wave number

γ = specific heat ratio

δ = boundary-layer thickness, mm

ε = forcing amplitude

μ = dynamic viscosity, Pa·s

ρ = density, kg/m^3

τ_{ij} = viscous stress tensor, N/m^2

φ = phase angle, radians

Subscripts

w = wall quantity

∞ = freestream quantity

Superscripts

– = mean quantity

′ = fluctuating quantity

I. Introduction

The performance of a hypersonic vehicle is significantly affected by the boundary-layer laminar–turbulent transition, which can greatly increase the surface heating and frictional drag and thus considerably decrease the vehicle's payload capacity [1]. In a weak-disturbance environment that is frequently encountered by a hypersonic vehicle, the path to transition comprises three stages: receptivity, linear eigenmode growth, and nonlinear breakdown to turbulence [2–4].

The transition mechanisms of hypersonic boundary layers are much more complex and much less understood than those of subsonic and moderate supersonic flows. That is, in addition to the first mode of hypersonic boundary layers, corresponding to the compressible counterpart of Tollmien–Schlichting waves (also referred to as the first mode), the second, third, and higher modes are involved and interpreted as trapped acoustic waves [5]. In hypersonic boundary-layer flows over a flat plate, mode F originates from the fast acoustic waves in the freestream, whereas mode S originates from the slow acoustic waves via the receptivity process near the leading edge. Excitation of the boundary-layer modes by freestream acoustic disturbances was investigated by Fedorov [6]. The modes can also be efficiently excited by a wall blowing-suction actuator [7]. The phase velocities of mode F and mode S intersect at the so-called synchronization point (SP), where the eigenfunctions of these modes are almost identical. Downstream of the SP, one mode experiences attenuation, whereas the other undergoes amplification. Both mode F and mode S can be unstable or only mode S is unstable with several growth rate maxima depending upon the flow conditions [8]. The low-frequency maximum occurring upstream of the SP (if exists) is associated with Mack's first mode, whereas the higher-frequency maxima downstream of the SP correspond to Mack's second, third, and higher modes. When these instabilities reach a certain amplitude, nonlinear secondary instabilities lead to breakdown to turbulence [4].

At hypersonic conditions, the second mode is the dominant instability because it exhibits a much larger growth rate than the first mode. For very high Mach numbers, the higher modes can be the leading unstable mode replacing the second mode. In contrast to

the first mode, which is most unstable as an oblique wave, the two-dimensional second mode is most amplified. The nature of the second mode allows the use of two-dimensional numerical simulations when only the linear regime of the instability is considered. To minimize and control the second-mode instabilities at the linear stage in hypersonic boundary layers, various passive and active control techniques have been proposed, such as local heating or cooling trips [9,10], roughness elements [11–13], porous coatings [14–21], CO_2 injection [22], and plasma actuators [23]. In some of these techniques, the positions of the element relative to the SP of mode F and mode S were critical for the control effectiveness. For example, the second mode was found to be amplified when a heating trip was located upstream of the SP, whereas the effect was reversed if it was placed downstream for a Mach 6 flat-plate boundary layer [10]. Duan et al. [11] performed two-dimensional numerical simulations on the stability of a Mach 5.92 flow over a flat plate with various roughness element locations. The results indicated that mode S was stabilized with the roughness located downstream of the SP. The damping effect was later confirmed by the wind tunnel experiment conducted by Fong et al. [12] on a flared cone with six roughness strips placed downstream of the SP associated with the most dangerous frequency. The experimental results demonstrated that the second-mode instability was completely damped on the rough cone. A similar trend has also been observed for local porous coatings [16,20].

Bountin et al. [24] demonstrated via direct numerical simulations (DNS) and experiments that the second mode can be strongly suppressed by a wavy surface with multiple small cavities. A series of shallow cavities that generated relatively stable recirculating flow regions and shear layers was used to stabilize the second-mode waves while avoiding the generation of any detrimental acoustic resonances. This idea was inspired by a numerical study that addressed the stability of hypersonic boundary layers over a compression corner [25]. It was shown that the second mode grew exponentially in the regions upstream of the separation bubble and downstream of the reattachment shock wave, whereas it remained neutral in the separation region. In contrast, the first-mode disturbance was found to be amplified only across the separation bubble. It can therefore be speculated that the cavity location relative to the SP of mode F and mode S is also important for wavy-wall stabilization. It was also observed that the flow structure in the

vicinity of a cavity element resembles that behind a local roughness. In this sense, the cavity and roughness elements are likely to share a similar influence on the second mode; however, in both cases the physical mechanism of the second-mode suppression remained incompletely understood.

Therefore, the objective of this study is to use DNS to investigate the effect of cavity locations on the stabilization of a hypersonic boundary layer at the linear stage. Two-dimensional simulations of a Mach 6 flat-plate flow over a local shallow cavity placed at various streamwise locations are performed to identify the SP's role. A parametric study of the effect of the cavity depth is then carried out. Last, an energy budget analysis of the evolution of the second-mode wave across the cavity is conducted to discern the damping mechanism.

II. Governing Equations

The governing equations are the compressible Navier–Stokes equations written in the following conservation form:

$$\frac{\partial \rho}{\partial t} + \frac{\partial \rho u_j}{\partial x_j} = 0 , \tag{1}$$

$$\frac{\partial \rho u_i}{\partial t} + \frac{\partial \rho u_i u_j}{\partial x_j} = -\frac{\partial p}{\partial x_i} - \frac{\partial \tau_{ij}}{\partial x_j} , \tag{2}$$

$$\frac{\partial \rho e}{\partial t} + \frac{\partial \rho h u_j}{\partial x_j} = -\frac{\partial \tau_{ij} u_i}{\partial x_j} - \frac{\partial q_j}{\partial x_j} , \tag{3}$$

where ρ is the density, u_i is the flow velocity, p is the pressure, e is the total energy per unit mass, h is the total enthalpy per unit mass, τ_{ij} is the viscous stress tensor, and q_j is the vector of heat conduction.

The fluid is assumed to be a perfect gas with the specific heat ratio $\gamma = 1.4$. The viscous stresses are modeled assuming a Newtonian fluid and Stokes' hypothesis, and the heat flux is calculated using Fourier's law. In terms of the transport properties, the dynamic viscosity is evaluated using Sutherland's law, and the coefficient of conductivity is determined via a constant Prandtl number $Pr = 0.72$.

III. Computational Details

A. Geometry and flow conditions

The schematic of a local cavity on a flat plate is shown in Fig. 1. The coordinate system is based on the origin located at the leading edge of the flat plate, with the x-axis in the horizontal direction and the y-axis in the vertical direction. The dimensions are chosen to be identical to those used by Bountin et al. [24]. The cavity had length l = 12 mm and depth d = 1.8 mm. The length-to-depth ratio (l/d) is 6.67 such that it could be regarded as a shallow cavity. It will be shown in Sec. IV A that these geometric parameters generate an open-type cavity flow devoid of unsteadiness or additional instabilities.

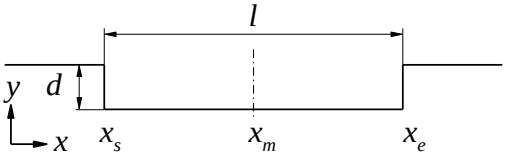

Fig. 1 Schematic of the cavity geometry.

The freestream conditions corresponding to the shock tunnel experiment of Bountin et al. [24] are given as follows: Mach number M_∞ = 6.0, unit Reynolds number Re_∞ = 10.5 × 10^6 m^{-1}, and static temperature T_∞ = 43.18 K. The flow density, velocities, pressure, and temperature are nondimensionalized by ρ_∞, u_∞, $\rho_\infty u_\infty^2$, and T_∞, respectively.

B. Flow solver

The numerical simulations are performed with a multiblock parallel finite-volume CFD code called PHAROS [26], which has been successfully applied to hypersonic thermochemical nonequilibrium simulations over capsule, double-cone, and hollow-cylinder/flare configurations [27–30]. In this study, PHAROS is extended to a higher-order accuracy for hypersonic transition simulations. The inviscid terms are calculated using the modified Steger–Warming scheme [31]. In this scheme, the split Jacobian matrices on cell faces are evaluated using an arithmetic average of the dependent variables in regions of small pressure gradient magnitude (e.g., inside the boundary layer) and a simple upwind approach in the vicinity of shock waves. To achieve a higher order, a ninth-order upwind scheme is used to reconstruct dependent variables in smooth regions, whereas the second-

order MUSCL reconstruction [32] with the van Leer slope limiter is used near discontinuities. Using this strategy, numerical oscillations caused by the leading edge and the shock wave can be eliminated, while the flow properties inside the boundary layer and near the cavity are well resolved with a low numerical dissipation. The viscous fluxes are calculated using the second-order central difference scheme.

C. Boundary conditions and simulation strategy

The computational domain extends from x = 0 mm to x = 250 mm and from y = 0 mm to y = 60 mm. The grid points in the streamwise direction between x = 0 and 200 mm are uniformly distributed, whereas the grid in the vertical direction is clustered near the wall to resolve the boundary layer. Note that the inflow boundary is located at the leading edge of the flat plate (i.e., x = 0 mm), where the freestream conditions are implemented. Downstream of x = 200 mm, the grid spacing gradually becomes coarse to rapidly damp the disturbances in the boundary layer, which allows the use of a simple extrapolation boundary condition at the exit boundary. No penetration and no slip conditions are used at the wall except in the blowing-suction region. In addition, the wall is assumed to be isothermal with T_w = 293 K.

The computational mesh is constructed with 1500 and 200 nodes in the x and y directions, respectively. Approximately 100 grid points are located within the boundary layer. 100 × 100 nodes are distributed in the domain of the separated flow for simulations that involved cavities. Grid independence was verified with a finer grid of 3000 × 400 nodes in the main domain and 200 × 200 nodes inside the cavity (see Fig. 2).

The simulation strategy consisted of two steps. First, the steady base flow is computed with a large Courant–Friedrichs–Lewy (CFL) number of 1000 to achieve fast convergence using the implicit line relaxation method [33]. In the second step, after disturbances are introduced using a local blowing-suction actuator on the wall, time-accurate unsteady simulations are performed using an explicit third-order Runge–Kutta method. The induced wall-normal mass flux by the actuator is determined by

$$\frac{\rho_w v_w}{\rho_\infty u_\infty} = \varepsilon \sin\left(2\pi \frac{x - x_1}{x_2 - x_1}\right) \sin\left(2\pi f t\right), \tag{4}$$

where the subscript w represents the wall quantities, x_1 = 10 mm and x_2 = 15 mm are the boundaries of the blowing-suction region, ε is the forcing amplitude, and f = 138.74 kHz is the forcing frequency. It will be shown later that this frequency results in a well-defined SP that is sufficiently distant from the actuator. Meanwhile, the induced disturbances experience a strong second-mode amplification within the computational domain. The forcing amplitude is set to $\varepsilon = 10^{-3}$ to ensure the linear evolution of the excited disturbances.

In this study, four cases with different cavity locations are considered: x_m = 0.04, 0.08, 0.12, and 0.16 m. For the wall blowing-suction actuator with f = 138.74 kHz, the cavity is located upstream of the SP of mode F and mode S for cases 1 and 2, whereas it is placed downstream of the SP for cases 3 and 4. The ratios of the cavity depth to the local boundary-layer thickness (d/δ) at x_m = 0.04, 0.08, 0.12, and 0.16 are 1.41, 1.00, 0.82, and 0.71, respectively (with the corresponding boundary-layer thickness of 1.28, 1.80, 2.20, and 2.54 mm).

To study the effect of cavity depth on suppressing the second mode, three additional cases are considered with d = 1.5, 2.1, and 2.4 mm at a fixed cavity location of x_m = 0.12. However, the cavity length remains unchanged. A large cavity length-to-depth ratio may lead to strong self-sustained oscillations and significant modification of the base flow. For the same reason, a shallower cavity (e.g., d < 1.5 mm) is not considered here. The effect of cavity length will be addressed in a future study.

D. Validation

To evaluate the accuracy of the present simulations, the results for the baseline flat-plate case are compared with the DNS data of Zhao et al. [10] and the predictions from linear stability theory (LST). The time series of fluctuating pressure at the wall is processed by Fourier transformation to obtain the fluctuating pressure amplitude $|p'|$ and phase angle φ'. In a spatial stability problem, the local wave number α and phase velocity c can be defined as

$$\alpha_r = \sqrt{\frac{\mu_\infty x}{\rho_\infty u_\infty}} \frac{d\varphi'}{dx}, \tag{5}$$

$$\alpha_i = -\sqrt{\frac{\mu_\infty x}{\rho_\infty u_\infty}} \frac{1}{|p'|} \frac{d|p'|}{dx}, \tag{6}$$

$$c = \frac{2\pi f}{u_\infty} \Big/ \frac{d\varphi'}{dx}, \tag{7}$$

where μ is the dynamic viscosity, and α_r and α_i are the real and imaginary parts of α, respectively. A mode is unstable when $\alpha_i < 0$, and it is stable when $\alpha_i > 0$.

Figure 2 illustrates the good agreement between the calculated distribution of $|p'|$ along the surface with that predicted by Zhao et al. [10] under the same flow conditions. In Ref. [10], DNS were performed using a fifth-order upwind compact scheme and a sixth-order central difference scheme to discretize the inviscid and viscous fluxes, respectively. The strong modulations of $|p'|$ downstream of the actuator can be attributed to the coexistence of mode F, mode S, acoustic waves, and entropy and vorticity waves [7]. As the disturbances propagate further downstream, $|p'|$ experiences an exponential increase starting from $x \approx 0.10$ m and reaches its maximum at $x \approx 0.15$ m.

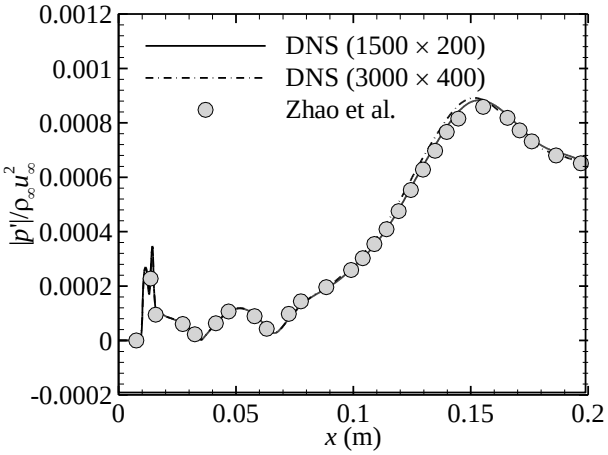

Fig. 2 Comparison of the fluctuating pressure amplitude obtained from the current DNS and that predicted by Zhao et al. [10].

Figure 3 compares the imaginary part of wave number α_i and phase velocity c obtained from the current DNS with those of mode F and mode S from LST. According to the LST predictions, mode F is always stable, whereas mode S is unstable from $x = 0.044$ m. The SP of mode F and mode S corresponding to $f = 138.74$ kHz is located at $x = 0.105$ m. Across the SP, mode S evolves from the first to the second mode and becomes dominant further downstream. Strong oscillations of α_i and c obtained from DNS downstream of the actuator are also caused by the coexistence of different modes. In the second-mode amplification

region, both α_i and c agree well with those of mode S from LST. When $x > 0.14$ m, the numerical result is more stable than that predicted by LST, which is caused by the nonparallel flow effects [7].

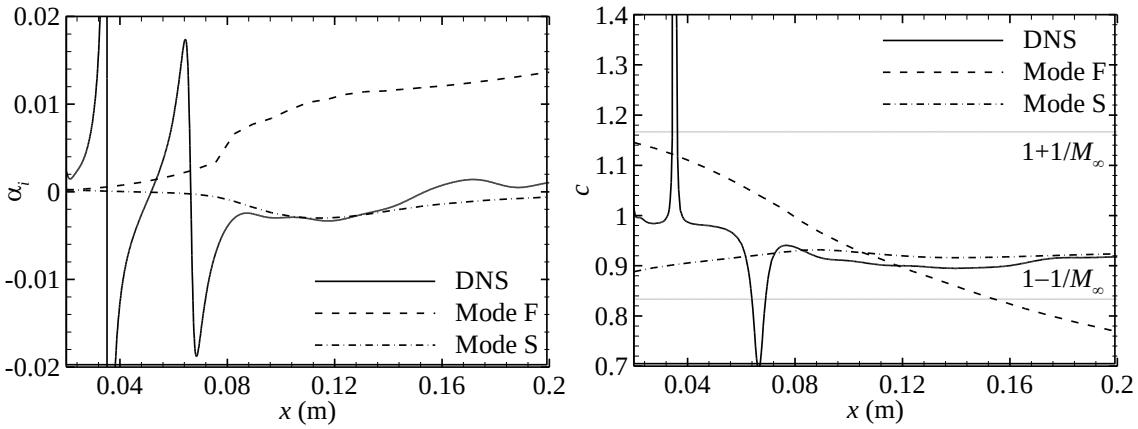

a) Imaginary part of wave number b) Phase velocity

Fig. 3 Comparison of the imaginary part of wave number and phase velocity obtained from the current DNS and those of mode F and mode S from LST.

IV. Results

A. Steady solution

The simulated steady base flow around the cavity for case 1 is shown in Fig. 4. A weak shock wave is generated near the flat-plate leading edge due to the viscous interaction, as seen from the pressure contour. The streamline pattern shows that the flow separates from the leading edge of the cavity and generates a shear layer that bridges the length of the cavity. A compression wave can be seen near the cavity trailing edge, which is induced by the shear-layer impingement. Notably, no self-sustaining oscillations arises in the base flow, and the steady-state flow structures for cases 2–4 are similar to those for case 1.

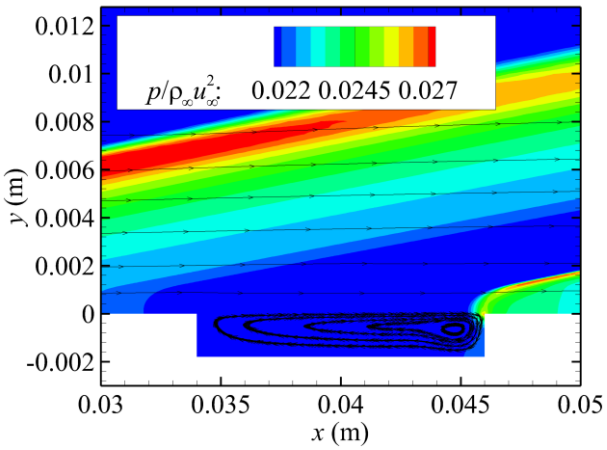

Fig. 4 Pressure contour and streamline pattern around the cavity for case 1.

Figure 5 shows the streamwise velocity profiles in the wall-normal direction at different locations for case 1. The baseline flat-plate results are also plotted for comparison. Clearly, the flow is largely unaffected upstream of the cavity. At x = 0.04 m located at the middle of the cavity, the velocity profile is strongly distorted, presenting a thinner boundary layer and a nonzero velocity at y = 0 m. Note that the velocity distribution inside the cavity is also shown. Most importantly, the existence of the shear layer reduces the magnitude of the wall-normal derivatives of the streamwise velocity. It will be demonstrated later that this is critical to the cavity's ability to suppress the second-mode instabilities.

Downstream of the cavity, deviation from the baseline results decreases, and the baseline profile is eventually reestablished after x = 0.08 m. The results indicate that the cavity has only local effects on the steady base flow, similar to what was observed in the numerical study of hypersonic flows over a local roughness element [12]. Although not shown here, the boundary-layer profiles for the other cases are similar. In fact, as the boundary-layer thickness increases, the cavity-mediated distortion effect is weakened.

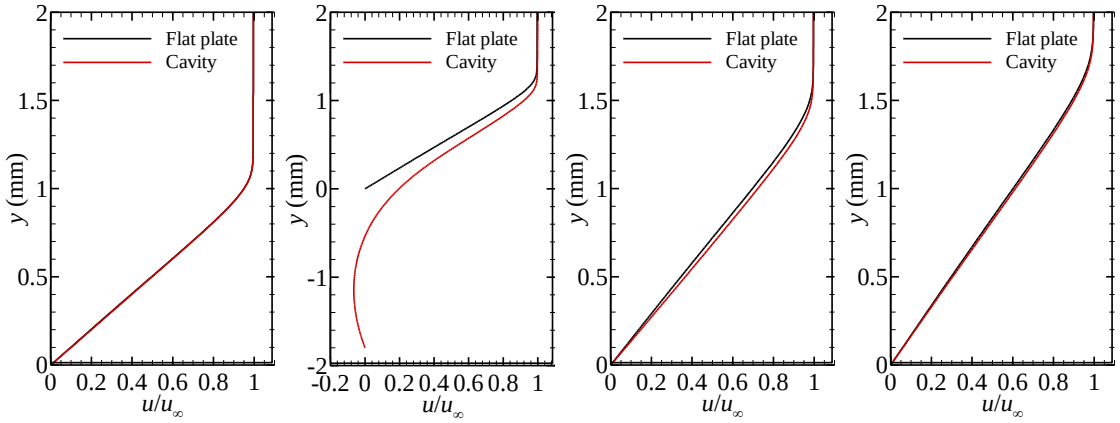

a) x = 0.03 m b) x = 0.04 m c) x = 0.06 m d) x = 0.08 m

Fig. 5 Distributions of streamwise velocity in the wall-normal direction at different locations for case 1.

B. Effect of cavity location on boundary-layer stability

Figure 6 shows the distributions of $|p'|$ along the surface for different cases. The development of $|p'|$ is clearly unaffected upstream of the cavity. However, when the cavity is placed upstream of the SP (cases 1 and 2), the maximum amplitude is increased compared with the baseline value. In contrast, the second mode is stabilized when the cavity is located slightly downstream of the SP (case 3). However, as the cavity moves further downstream (case 4), the maximum fluctuating pressure is again amplified. No significant change is seen in the fluctuation across the cavity for cases 1 and 2, whereas it is significantly reduced across the cavity for cases 3 and 4.

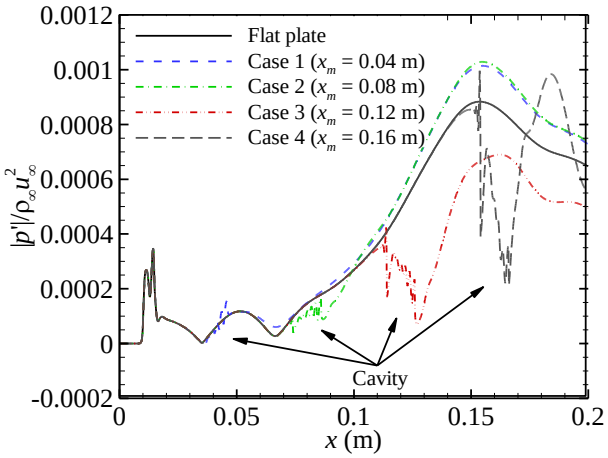

Fig. 6 Distributions of the fluctuating pressure amplitude along the surface (y = 0 m) for different cases.

Figure 7 compares the imaginary parts of the wave number for different cases with the baseline flat-plate result and those of mode F and mode S obtained from LST. Again, the cavity has only local effects on the development of disturbances, especially for cases 1 and 2. The baseline result is recovered further downstream of the cavity, and the numerical results agree well with the theoretical prediction of mode S. Note that the growth rates immediately after the cavity are much larger than those for the flat plate for cases 3 and 4; these large growth rates correspond to the steep increase in the fluctuating pressure amplitude as shown in Fig. 6. For case 4, even though the disturbances are significantly reduced across the cavity, the growth rate after the cavity increases so much that the perturbation amplitude experiences a strong growth and exceeds the flat-plate result.

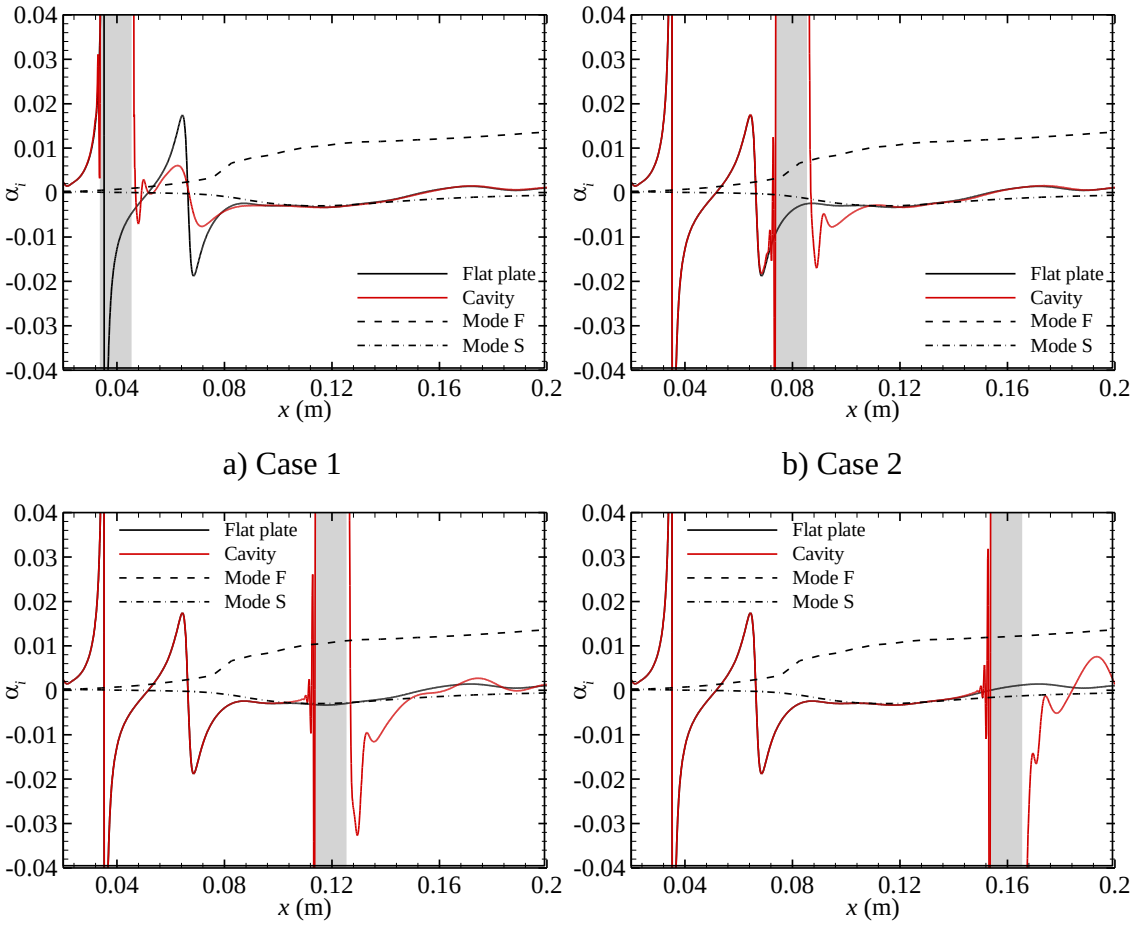

a) Case 1 b) Case 2

0.04
0.03
0.02
0.01
0
-0.01
-0.02
-0.03
-0.04
α_i
0.04
0.08
0.12
0.16
0.2
x (m)
Flat plate
Cavity
Mode F
Mode S

c) Case 3 d) Case 4

Fig. 7 Distributions of the imaginary part of wave number along the surface (y = 0 m) for different cases. Grey-shaded region indicates location of cavity.

These findings help to explain the numerical results of Bountin et al. [24], as their study showed that the second mode was damped by the wavy surface between 110 and 150 kHz, whereas the disturbance amplitude increased for frequencies below 110 kHz and remained almost unchanged for frequencies above 150 kHz. It has been well-established that the location of the SP is inversely related to the frequency [11], such that most cavities of the wavy surface were located upstream of the SP for relatively low frequencies. As a result, the second mode is amplified. For high frequencies, cavities were located further downstream of the corresponding SP, which was also detrimental to the overall stabilization effect.

C. Effect of cavity depth on boundary-layer stability

The effect of cavity depth on suppressing the second mode is studied for case 3 and for three additional cases: cases 3a (d = 1.5 mm), 3b (d = 2.1 mm), and 3c (d = 2.4 mm). The cavity depth for case 3 is 1.8 mm, and the local boundary-layer thickness is 2.2 mm at the middle of the cavity obtained from the baseline simulation. Thus, one additional case is shallower than case 3, and two are deeper; the cavity depth of case 3c is even greater than the local boundary-layer thickness.

Figure 8 shows the distributions of $|p'|$ along the surface for cases 3 and 3a–c, and the baseline flat-plate result is also plotted for direct comparison. It can be seen that when the cavity depth is less than the local boundary-layer thickness, the deeper cavity induces a stronger damping effect on the second mode. However, when the cavity depth is greater than the local boundary-layer thickness (i.e., case 3c), the damping effect is weakened. For cases 3a, 3, and 3b, the maximum fluctuating pressure amplitudes are reduced by 1.9%, 21.9 %, and 29.5%, respectively, compared with the flat-plate value, whereas the reduction is 23.8% for case 3c. It is indicated that the cavity depth must be carefully selected according to local boundary-layer conditions to effectively suppress the second mode.

A similar trend has been demonstrated for hypersonic boundary layers over ultrasonic absorptive coatings [14,15]. It was shown that the second-mode growth rate oscillates with the pore depth due to phase cancellation or reinforcement associated with reflection of acoustic waves from the bottom of pores. Notably, the flow structures inside an individual pore with l/d of the order of 0.1 and a shallow cavity (i.e., $l/d > 3$) can be very different.

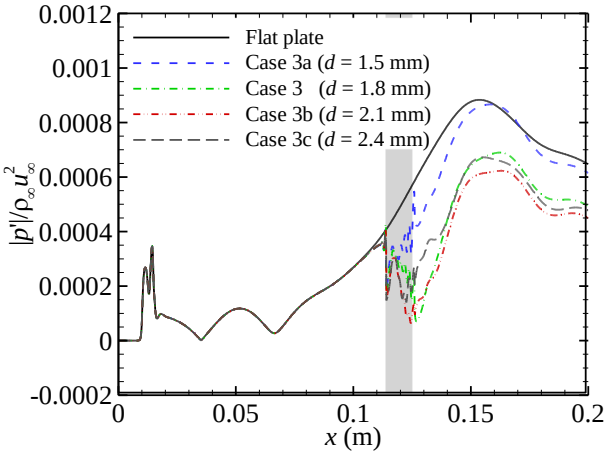

Fig. 8 Distributions of the fluctuating pressure amplitude along the surface (y = 0 m) for different cases. Grey-shaded region indicates location of cavity.

D. Physical mechanism of second-mode damping

As shown in Fig. 6, the second mode is strongly damped across the cavity placed downstream of the SP. To illustrate the development of the second-mode wave in the vicinity of the cavity, Fig. 9 shows the instantaneous contours of the fluctuating pressure for cases 3 and 4 and for the flat-plate case.

For the baseline case, the disturbances in the boundary layer after x = 0.105 m correspond to the second-mode wave, which propagates downstream at a phase velocity slightly lower than the velocity at the boundary-layer edge (see Fig. 3b). The second-mode wave is reflected between the wall and the sonic line (relative to the phase velocity) and is interpreted as trapped acoustic waves that induce the two-cell structures of the fluctuating pressure field with a zero-crossing near the sonic line.

The basic feature of cases 3 and 4 are similar to the flat-plate result upstream and downstream of the cavity; however, the pressure fluctuations are strongly distorted around the cavity. Interestingly, the fluctuating pressure across the cavity passes through the zero

axis (i.e., $p' = 0$) twice in the y direction, which might suggest the existence of a third mode, according to the theory of Mack [34]. However, it is important to note that the fluctuations are trapped by the waves emanating from the leading edge of the cavity, whereas the Mack modes are unbounded in the wall-normal direction.

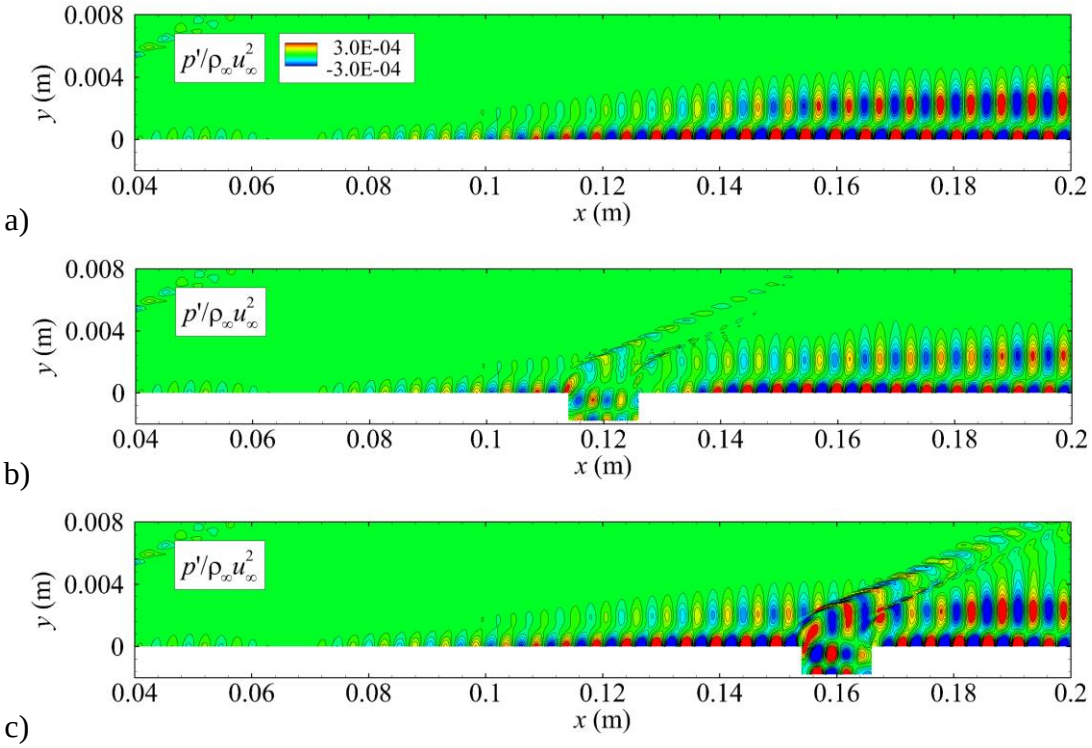

Fig. 9 Instantaneous snapshots of the fluctuating pressure for a) flat plate, b) case 3, and c) case 4 (not to scale).

Next, the physical mechanism that drives the observed second-mode damping across the cavity is analyzed by quantifying the disturbance using an energy norm and by evaluating the contribution budget in the energy balance equation.

There is no unique definition for disturbance energy. In this study, the energy norm proposed by Chu [35], Mack [34], and Hanifi et al. [36] is used,

$$E = \frac{1}{2}\left(\bar{\rho} u_i' u_i' + \frac{\bar{p}}{\bar{\rho}^2} \rho' \rho' + \frac{\bar{\rho} C_v}{\bar{T}} T' T' \right), \tag{8}$$

where C_v is the specific heat at constant volume. This definition includes the kinetic energy of the disturbance and a strictly positive term for the thermodynamic fluctuating quantities,

which has been widely used to study the non-modal behavior of compressible flow dynamics [37,38].

To obtain the disturbance energy equation, the transport equations of the relevant fluctuating quantities are first derived by linearizing the flow governing equations given in Sec. II, which can be written in the following form:

$$\frac{\partial \rho'}{\partial t} + \bar{u}_j \frac{\partial \rho'}{\partial x_j} = -u_j' \frac{\partial \bar{\rho}}{\partial x_j} - \left(\rho \frac{\partial u_j}{\partial x_j} \right)', \tag{9}$$

$$\frac{\partial u_i'}{\partial t} + \bar{u}_j \frac{\partial u_i'}{\partial x_j} = -\frac{\left(\rho u_j\right)'}{\bar{\rho}} \frac{\partial \bar{u}_i}{\partial x_j} - \frac{1}{\bar{\rho}} \frac{\partial p'}{\partial x_i} - \frac{1}{\bar{\rho}} \frac{\partial \tau_{ij}'}{\partial x_j}, \tag{10}$$

$$\frac{\partial T'}{\partial t} + \bar{u}_j \frac{\partial T'}{\partial x_j} = -u_j' \frac{\partial \bar{T}}{\partial x_j} - (\gamma - 1)\left(T \frac{\partial u_j}{\partial x_j} \right)' - \frac{1}{\bar{\rho} C_v} \left(\tau_{ij} \frac{\partial u_i}{\partial x_j} + \frac{\partial q_j}{\partial x_j} \right)'. \tag{11}$$

Eqs. (9)–(11) are then multiplied by $\bar{p}\rho'/\bar{\rho}^2$, $\bar{\rho}u_i'$, and $\bar{\rho}C_v T'/\bar{T}$, respectively, and summed. The resulting equation is averaged over one period corresponding to the actuating frequency to eliminate the time derivative term, which can be written as

$$\bar{u}_j \frac{\partial \bar{E}}{\partial x_j} = \mathrm{P} + \mathrm{T} + \mathrm{V}, \tag{12}$$

$$\mathrm{P} = \underbrace{-\overline{u_i' \left(\rho u_j\right)'} \frac{\partial \bar{u}_i}{\partial x_j}}_{\text{Reynolds stress production}} \underbrace{- \frac{\bar{p}}{\bar{\rho}^2} \overline{\rho' u_j'} \frac{\partial \bar{\rho}}{\partial x_j} - \frac{\bar{\rho} C_v}{\bar{T}} \overline{T' u_j'} \frac{\partial \bar{T}}{\partial x_j}}_{\text{Thermal production}}, \tag{13}$$

$$\mathrm{T} = -\overline{u_i' \frac{\partial p'}{\partial x_i}} - \frac{\bar{p}}{\bar{\rho}^2} \overline{\rho' \left(\rho \frac{\partial u_j}{\partial x_j} \right)'} - \frac{\bar{\rho} R}{\bar{T}} \overline{T' \left(T \frac{\partial u_j}{\partial x_j} \right)'}, \tag{14}$$

$$\mathrm{V} = -\overline{u_i' \frac{\partial \tau_{ij}'}{\partial x_j}} - \frac{1}{\bar{T}} \overline{T' \left(\tau_{ij} \frac{\partial u_i}{\partial x_j} \right)'} - \frac{1}{\bar{T}} \overline{T' \frac{\partial q_j'}{\partial x_j}}. \tag{15}$$

In these expressions, P, T, and V are the production, transfer, and viscous terms, respectively. The mean flow is assumed to be parallel to obtain the left hand side of the equation representing the advection of the disturbance energy by the mean velocity, which is an assumption that generally holds, except near the leading and trailing edges of the cavity. Nevertheless, the streamwise derivatives of the mean quantities are kept on the right hand side of the equation. P can be further categorized into two terms (Eq. (13)), according to Franko [39]. The Reynolds stress production is developed from the momentum equation

and represents the work done by the Reynolds stress on the mean velocity gradient, whereas the thermal production denotes the energy transfer due to mean density and temperature gradients. T combines the contributions from energy transport due to fluctuations and dilatation as a result of compressibility (Eq. (14)), and V accounts for the diffusion and dissipation effects associated with molecular transport (Eq. (15)). Note that such an energy budget analysis cannot distinguish different eigenmodes; however, it is mainly applied downstream of the SP where the dominating disturbance is the second mode.

Figure 10 shows the instantaneous contours of the disturbance energy for different cases. For the flat-plate case, the disturbance energy is mainly distributed in two regions. The disturbance energy in the upper region of the boundary layer is observed even upstream of the SP and continues to increase until the end of the computational domain. In contrast, the disturbance energy confined in the lower region is only evident downstream of the SP and peaks near x = 0.15 m, near the location of the peak obtained from the surface fluctuating pressure amplitude (see Fig. 2). Close examination reveals that the fluctuating density and temperature contribute to the energy distribution at the edge of the boundary layer, whereas the disturbance energy near the wall mainly consists of the kinetic energy. For the cavity cases, the disturbance energy distributions are similar to those for the flat plate upstream and downstream of the cavity; however, the disturbance energy located in the lower region of the boundary layer is significantly damped across the cavity.

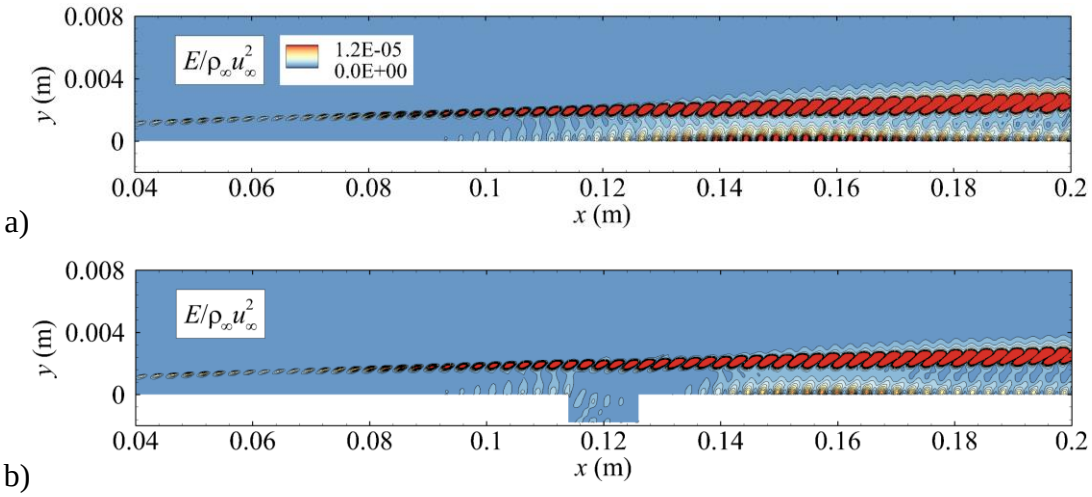

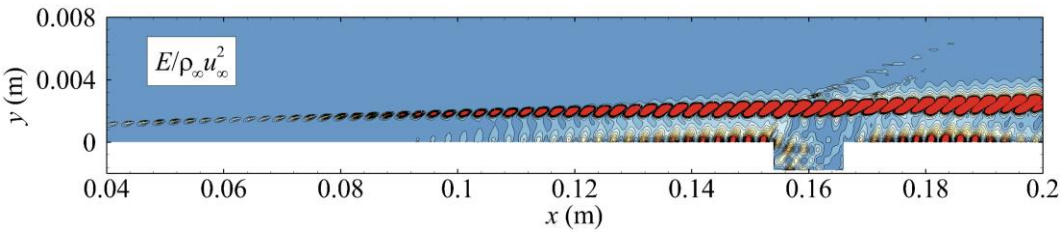

c)

Fig. 10 Instantaneous snapshots of the disturbance energy for a) flat plate, b) case 3, and c) case 4 (not to scale).

To understand the physical mechanism that drives the damping of the disturbance energy, the energy budget is examined in the wall-normal direction at x = 0.12 m downstream of the SP for the flat plate and case 3, as shown in Fig. 11. The locations of the critical layer and sonic line are also marked. Note that the critical layer is defined as the location at which the mean streamwise velocity is equal to the phase velocity of the disturbance.

Considering the flat-plate result first, the thermal production has the largest magnitude and is localized near the critical layer, whereas the Reynolds stress production has a moderate constant value throughout the boundary layer. The transfer term serves as a sink in most part of the boundary layer and is positive only near the wall. Furthermore, the viscous term has two peaks near the edge and bottom of the boundary layer. As a consequence, the net energy source is positive in two regions: in the vicinity of the critical layer and between the sonic line and the surface. This positive energy source indicates that the disturbance energy is amplified in the streamwise direction. In fact, the amplification of the disturbance energy near the critical layer is dominated by thermal production. Although the transfer term has a peak value near the wall, it is largely balanced by the viscous term such that the second amplification region of the disturbance energy is driven by the Reynolds stress production. Similar features were also reported by Franko [39].

For the cavity case, the profiles of the thermal production, transfer, and viscous terms are similar to those for the flat plate, despite the significantly reduced magnitudes of these terms. Most importantly, the Reynolds stress production is almost eliminated; this causes the net energy source between the sonic line and the wall to become negative, and thus the disturbance energy is reduced in the streamwise direction, analogous to the damping effect

observed above. It could therefore be concluded that the second-mode suppression across the cavity arises from the reduction of the Reynolds stress production.

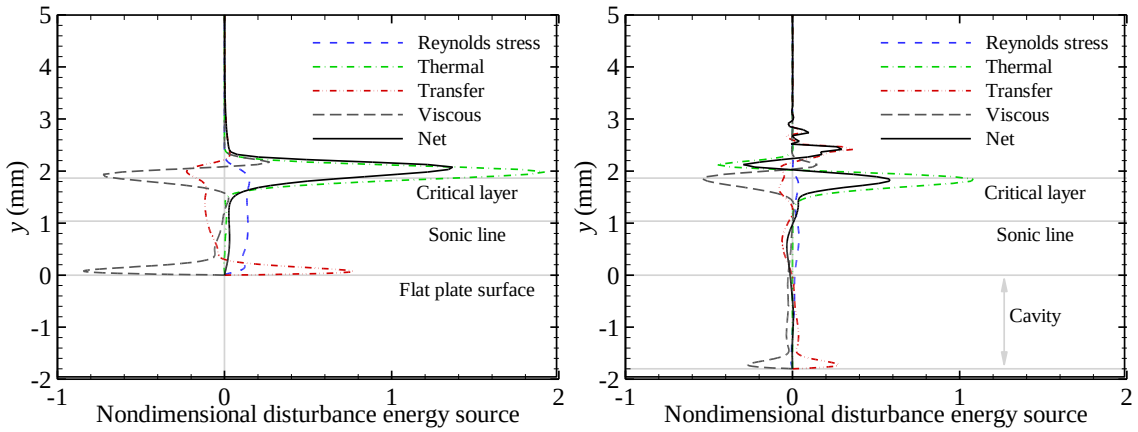

a) Flat plate b) Case 3

Fig. 11 Disturbance energy budget at x = 0.12 m for different cases. Vertical grey lines indicate zero disturbance energy source.

Given that the Reynolds stress production is related to the mean velocity gradient, it is of interest to examine how it is influenced by the cavity. Figure 12 shows the profiles of the mean flow velocity and its wall-normal gradient at x = 0.12 m. Note that the wall-normal mean velocity gradient is much larger than its streamwise counterpart. It can also be seen that the mean velocity distributions are similar to those previously observed for case 1 (see Fig. 5). Moreover, due to the existence of the shear layer bridging the leading and trailing edges of the cavity, the velocity gradient is significantly reduced in the region between the sonic line and the flat-plate surface. Consequently, the Reynolds stress production is decreased, and the disturbance energy is damped in this region. Although not shown here, the behaviors of the energy source terms at x = 0.16 m for the flat plate and case 4 are similar to those shown in Fig. 11, and the damping mechanism also results from reduction of the Reynolds stress production.

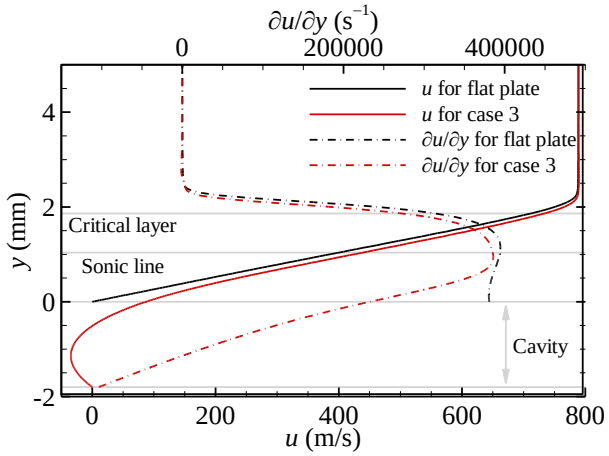

Fig. 12 Profiles of the mean streamwise velocity and corresponding wall-normal gradient at x = 0.12 m for flat plate and case 3.

Figure 13 shows the disturbance energy budget at x = 0.14 m for case 3. It can be seen that the Reynolds stress production term has reestablished downstream of the cavity such that the disturbance energy grows again. The regrowth of the second mode downstream of the cavity is considered to be unimportant. In fact, a series of shallow cavities could be implemented such that the magnitude of the disturbance energy near the wall can remain at a relatively low level. However, the disturbance near the critical layer still increases across the cavity, albeit at a lower growth rate, thus indicating that a cavity could only effectively control the disturbance near the wall. Eventually, laminar-turbulent transition would occur as the disturbance near the critical layer reaches a certain level. It is suggested that natural transition simulations should be performed to closely examine the role of the two amplification regions of disturbance energy in the process of laminar–turbulent transition dominated by the second-mode instabilities.

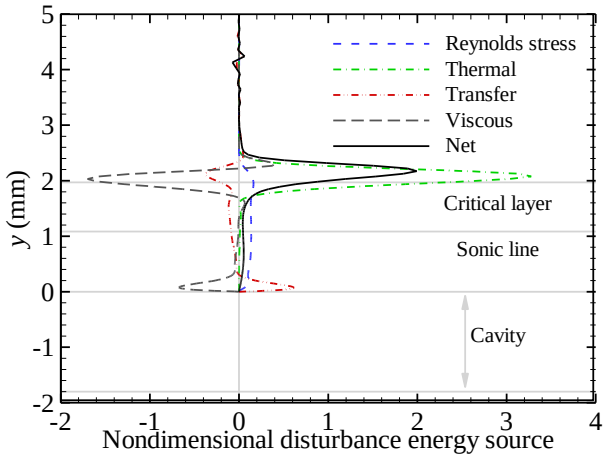

Fig. 13 Disturbance energy budget at x = 0.14 m for case 3. Vertical grey lines indicate zero disturbance energy source.

These findings reveal that effective suppression of the second mode can be achieved by reduction of the mean velocity gradient, which explains the damping mechanism of many laminar control techniques. For instance, stabilization using a local roughness element generates a similar separated flow region behind the roughness such that the velocity gradient is reduced. Another example is positioning a heating trip downstream of the SP. In this case, the local boundary layer thickness is increased, which also results in a lower velocity gradient. A more detailed examination of various laminar control techniques from the perspective of energy balance will be conducted in a future study.

V. Conclusions

The stabilization of a hypersonic boundary layer with a local two-dimensional shallow cavity is investigated using DNS. Four cases are considered with the cavity located upstream or downstream of the SP of mode F and mode S. The results indicate that the cavity location plays an important role in the development of mode S excited by wall blowing-suction. When the cavity is located upstream or further downstream of the SP, the second mode is destabilized; the second mode is stabilized only if the cavity is placed closely downstream of the SP. The stabilization effect of the relative location between the cavity and the SP is similar to those for local heating trips, roughness elements, and porous coatings. It is suggested that an efficient way to stabilize the boundary layer is to position

a local cavity in the near-downstream region of the SP corresponding to the most amplified frequency.

The effect of the cavity depth on suppression of the second mode is also studied. It is shown that when the cavity depth is less than the local boundary-layer thickness, the stabilization effect of the second mode is strengthened as the cavity depth increases. However, the damping effect is weakened if the cavity depth is larger than the boundary-layer thickness. This trend is similar to that for hypersonic boundary layers over ultrasonically absorptive coatings, despite the fact that the flow structures can be very different.

The evolution of the second-mode wave across the cavity when placed downstream of the SP shows that the disturbance is significantly damped across the cavity. The second-mode wave becomes the third mode when propagating across the separation region, and the third-mode wave then reverts to the second mode downstream. The energy budget analysis for the flat-plate flow reveals that there are two disturbance energy amplification regions in the boundary layer: one is near the critical layer dominated by the thermal production associated with the mean density and temperature gradients, and the other is between the sonic line and the surface controlled by the Reynolds stress production, in terms of the work done by the Reynolds stress on the mean velocity gradient. The second-mode damping across the cavity is caused by the presence of a shear layer bridging the leading and trailing edges of the cavity, which reduces the mean flow velocity gradient and thus attenuates the Reynolds stress production.

Acknowledgments

The authors would like to thank the Hong Kong Research Grants Council (no. C5010-14E, no. 152041/18E, and no. 152065/19E) the National Natural Science Foundation of China (no. 11772284) for financial support. The authors are also grateful to the National Supercomputer Center in Tianjin for providing computational resource.

References

[1] Schneider, S. P., "Flight Data for Boundary-Layer Transition at Hypersonic and Supersonic Speeds," *Journal of Spacecraft and Rockets*, Vol. 36, No. 1, 1999, pp. 8–20.

[2] Morkovin M. V., "Transition at Hypersonic Speeds," NASA CR 178315, 1987.

[3] Reshotko E., "Transition issues for atmospheric entry," *Journal of Spacecraft and Rockets*, Vol. 45, No. 2, 2008, 161–164.

[4] Zhong, X. and Wang, X., "Direct Numerical Simulation on the Receptivity, Instability, and Transition of Hypersonic Boundary Layers,". *Annual Review of Fluid Mechanics*, Vol. 44, 2012, pp. 527–561.

[5] Fedorov, A. and Tumin, A., "Transition and Stability of High-Speed Boundary Layers,". *Annual Review of Fluid Mechanics*, Vol. 43, 2011, pp. 79–95.

[6] Fedorov, A. V., "Receptivity of a high-speed boundary layer to acoustic disturbances," *Journal of Fluid Mechanics*, Vol. 491, 2003, pp. 101–129.

[7] Wang, X., Zhong, X., and Ma, Y., "Response of a Hypersonic Boundary Layer to Wall Blowing-Suction," *AIAA Journal*, Vol. 49, No. 7, 2011, pp. 1336–1353.

[8] Fedorov, A. and Tumin, A., "High-Speed Boundary-Layer Instability: Old Terminology and a New Framework,". *AIAA Journal*, Vol. 49, No. 8, 2011, pp. 1647–1657.

[9] Fedorov, A., Soudakov, V., Egorov, I., Sidorenko, A., Gromyko, Y., Bountin, D., Polivanov, P., and Maslov, A., "High-Speed Boundary-Layer Stability on a Cone with Localized Wall Heating or Cooling," *AIAA Journal*, Vol. 53, No. 9, 2015, pp. 2512–2524.

[10] Zhao, R., Wen, C.-Y., Tian, X. D., Long, T. H., and Yuan, W., "Numerical Simulation of Local Wall Heating and Cooling Effect on the Stability of a Hypersonic Boundary Layer," *International Journal of Heat and Mass Transfer*, Vol. 121, 2018, pp. 986–998.

[11] Duan, L., Wang, X., and Zhong, X., "Stabilization of a Mach 5.92 Boundary Layer by Two-Dimensional Finite-Height Roughness," *AIAA Journal*, Vol. 51, No. 1, 2013, pp. 266–270.

[12] Fong, K. D., Wang, X., Huang, Y., Zhong, X., McKiernan, G. R., Fisher, R. A., and Schneider, S. P., "Second Mode Suppression in Hypersonic Boundary Layer by Roughness: Design and Experiments," *AIAA Journal*, Vol. 53, No. 10, 2015, pp. 3138–3143.

[13] Tang, Q., Zhu, Y., Chen, X., and Lee, C., "Development of Second-Mode Instability in a Mach 6 Flat Plate Boundary Layer with Two-Dimensional Roughness," *Physics of Fluids*, Vol. 28, 2015, 064105.

[14] Fedorov, A. V., Malmuth, N. D., and Hornung, H. G., "Stabilization of Hypersonic Boundary Layers by Porous Coatings," *AIAA Journal*, Vol. 39, No. 4, 2001, pp. 605–610.

[15] Brès, G. A., Inkman, M., Colonius, T., and Fedorov, A. V., "Second-Mode Attenuation and Cancellation by Porous Coatings in a High-Speed Boundary Layer," *Journal of Fluid Mechanics*, Vol. 726, May 2013, pp. 312–337.

[16] Wang, X. and Zhong, X., "The Stabilization of a Hypersonic Boundary Layer Using Local Sections of Porous Coating," *Physics of Fluids*, Vol. 24, 2012, 034105.

[17] Wartemann, V., Wagner, A., Giese, T., Eggers, T., and Hannemann, K., "Boundary-layer stabilization by means of ultrasonically absorptive material on a cone in hypersonic flow," *CEAS Space Journal*, Vol. 6, 2014, pp. 13-22.

[18] Zhao, R., Liu, T., Wen, C.-Y., Zhu, J., and Cheng L., "Theoretical Modeling and Optimization of Porous Coating for Hypersonic-Laminar-Flow Control," *AIAA Journal*, Vol. 56, No. 8, 2018, pp. 2942–2946.

[19] Zhao, R., Liu, T., Wen, C.-Y., Zhu, J., and Cheng, L., "Impedance-Near-Zero Acoustic Metasurface for Hypersonic Boundary-Layer Flow Stabilization," *Physical Review Applied*, Vol. 11, 2019, 044015.

[20] Zhao, R., Wen, C.-Y., Long, T. H., Tian, X. D., Zhou, L., and Wu, Y., "Spatial Direct Numerical Simulation of the Hypersonic Boundary-Layer Stabilization Using Porous Coatings," *AIAA Journal*, Vol. 57, No. 11, 2019, pp. 5061–5065.

[21] Tian, X. D., Long, T. H., Wen, C.-Y., and Zhao, R., "Reverse Design of Ultrasonic Absorptive Coating for Stabilizing Mack Modes in a High-Speed Boundary Layer," *AIAA Journal*, Vol. 57, No. 6, 2019, pp. 2264–2269.

[22] Wagnild, R. M., Candler, G. V., Leyva, I. A., Jewell, J. S., and Hornung, H. G., "Carbon Dioxide Injection for Hypervelocity Boundary Layer Stability," *48th AIAA Aerospace Sciences Meeting Including the New Horizons Forum and Aerospace Exposition*, AIAA Paper 2010-1244, 2010.

[23] Riherd, M., Roy, S., Balachandar, S., "Local stability effects of plasma actuation on a zero pressure gradient boundary layer," *Theoretical and Computational Fluid Dynamics*, 2014, Vol. 28, pp. 65–87.

[24] Bountin, D., Chimitov, T., Maslov, A., Novikov, A., Egorov, I., Fedorov, A., and Utyuzhnikov, S., "Stabilization of a Hypersonic Boundary Layer Using a Wavy Surface," *AIAA Journal*, Vol. 51, No. 5, 2013, pp. 1203–1210.

[25] Balakumar, P., Zhao, H., and Atkins, H., "Stability of Hypersonic Boundary Layers over a Compression Corner," *AIAA Journal*, Vol. 43, No. 4, 2005, pp. 760–767.

[26] Hao, J., Wang, J., and Lee, C., "Numerical Study of Hypersonic Flows over Reentry Configurations with Different Chemical Nonequilibrium Models," *Acta Astronautica*, Vol. 126, 2016, pp. 1–10.

[27] Hao, J., Wang, J., and Lee, C., "Development of a Navier–Stokes Code for Hypersonic Nonequilibrium Simulations," *21st AIAA International Space Planes and Hypersonics Technologies Conference*, AIAA Paper 2017-2164, 2017.

[28] Hao, J., Wang, J., and Lee, C., "Numerical Simulation of High-Enthalpy Double-Cone Flows," *AIAA Journal*, Vol. 55, No. 7, 2017, pp. 2471–2475.

[29] Hao, J. and Wen, C.-Y., "Numerical Investigation of Oxygen Thermochemical Nonequilibrium on High-Enthalpy Double-Cone Flows", *International Journal of Heat and Mass Transfer*, Vol. 127, 2018, pp. 892–902.

[30] Hao, J., Wang, J., and Lee, C., "Numerical Simulation of High-Enthalpy Hollow-Cylinder/Flare Flows," *AIAA Journal*, Vol. 56, No. 8, 2018, pp. 3337–3341.

[31] MacCormack, R. W., *Numerical Computation of Compressible and Viscous Flow*, AIAA Education Series, AIAA, Reston, VA, 2014, pp. 181–185.

[32] Van Leer, B., "Towards the Ultimate Conservative Difference Scheme," *Journal of Computational Physics*, Vol. 32, No. 1, 1979, pp. 101–136.

[33] Wright, M. J., Candler, G. V., and Bose, D., "Data-Parallel Line Relaxation Method for the Navier–Stokes Equations," *AIAA Journal*, Vol. 36, No. 9, 1998, pp. 1603–1609.

[34] Mack, L. M., "Boundary-Layer Linear Stability Theory," AGARD Report No. 709, 1984.

[35] Chu, B.-T., "On the Energy Transfer to Small Disturbances in Fluid Flow (Part I)," *Acta Mechanica I,* Vol. 1, No. 3, 1965, pp. 215–234.

[36] Hanifi, A., Schmid, P. J., and Henningson, D. S., "Transient Growth in Compressible Boundary Layer Flow," *Physics of Fluids*, Vol. 8, No. 3, 1996, pp. 826–837.

[37] Tumin, A., and Reshotko, E., "Spatial Theory of Optimal Disturbances in Boundary Layers," *Physics of Fluids,* Vol. 13, No. 7, 2001, pp. 2097–2104.

[38] Nichols, J. W. and Lele, S. K., "Global modes and transient response of a cold supersonic jet," *Journal of Fluid Mechanics,* Vol. 669, 2011, pp. 225–241.

[39] Franko, K. J., "Linear and Nonlinear Processes in Hypersonic Boundary Layer Transition to Turbulence," Ph.D. Dissertation, Stanford Univ., Stanford, CA, 2011.